Article:
Kamkeng, A.D.N. and Wang, M. (2022) Long-term performance prediction of solid oxide electrolysis cell (SOEC) for CO2/H2O co-electrolysis considering structural degradation through modelling and simulation. Chemical Engineering Journal, 429. 132158. ISSN: 1385-8947

https://doi.org/10.1016/j.cej.2021.132158

Long-term performance prediction of solid oxide electrolysis cell (SOEC) for CO_2/H_2O co-electrolysis considering structural degradation through modelling and simulation

Ariane D. N. Kamkeng[a] and Meihong Wang[a,*]

[a]*Department of Chemical and Biological Engineering, University of Sheffield, Mappin Street, Sheffield, S1 3JD, United Kingdom.*

**Corresponding Author: Prof Meihong Wang, E-mail address: Meihong.Wang@sheffield.ac.uk*

Abstract

Solid oxide electrolysis cells (SOECs) are promising devices for CO_2 and H_2O co-electrolysis into syngas. Degradation occurring within SOECs is still of great concern for their commercial deployment. Therefore, it is important to understand the degradation mechanisms and optimize SOEC long-term operation. A 1-dimensional (1D) pseudo-dynamic model was developed for SOEC operating under CO_2/H_2O co-electrolysis and implemented in Aspen Plus® using Fortran® routines. The structural degradation of a typical SOEC material set: Ni-YSZ cathode, YSZ electrolyte and LSM-YSZ anode were also accounted for. The model was dynamically validated for different current densities (0.5, 0.75 and 1.0 A/cm^2). The effects of operating conditions and structural degradation on SOEC long-term electrochemical performance and syngas production are assessed. Performance prediction indicated that increasing the current density and operating temperature initially enhance SOEC performance. However, the operating voltage increases at faster rates at higher current densities and temperatures causing the syngas production efficiency to decrease due to higher power utilisation. Long-term SOEC degradation is mostly due to LSM-YSZ anode delamination with a degradation rate of 3.96 %/1000hrs at 750°C, 1 bar and 1.5 A/cm^2. Applying an anti-oxidant layer on the interconnect surface and adjusting La/Sr ratio in the A-site of LSM considerably reduce the degradation rate by roughly 78% at the anode.

Keywords

CO_2 Utilisation; Solid Oxide Electrolysis Cell (SOEC); Syngas; Degradation; Modelling and Simulation; Process analysis

Abbreviations

CGO: Ceria gadolinium oxide

FTS: Fischer-Tropsch synthesis

LSCF: Lanthanum strontium cobalt iron oxide

LSM: Lanthanum strontium manganite

LZO: Lanthanum zirconate oxide

RWGS: Reverse water gas shift

SEM: Scanning electron microscope

SOEC: Solid oxide electrolysis cell

SOFC: Solid oxide fuel cell

TPB: Triple phase boundary

YSZ: Yttria-stabilised zirconia

Nomenclature

A_{cell}: Cell active area (cm^2)

A_{YSZ}: YSZ surface area (m^2/g)

C: Temperature-independent constant

COS: Chromium oxide scale

d_i: Thickness of component i (cm)

D_{LSM}: LSM surface diffusion (cm^2/hr)

$E_{a,i}$: Component *i* activation energy (J/mol)

E_i: Activation energy for component *i* growth (J/mol)

E_{Sin}: Activation energy for sintering (J/mol)

F: Faraday constant (96,485 J/V.mol)

HHV_{in} and HHV_{out}: Inlet and outlet higher heating value (W)

I: Current (A)

j_0: Exchange current density (A/cm^2)

j: Current density (A/cm^2)

K_i: Adsorption constant

K_i^0: Standard adsorption constant

$K_{g,i}$: Weight gain rate for component *i* growth ($g/cm^4.hr$)

$K_{p,i}$: Parabolic constant for component *i* (cm^2/hr)

L_{TPB}: TPB length or TPB density (μm^{-2})

n: Number of electrons transferred per electrolysis

N_{cell}: Number of cells in SOEC stack

$\dot{N}_{in}$: Cathode inlet flowrate (mol/sec)

P_{cell}: Power utilisation per cell (W)

P_{std} and P: Standard and operating pressure (bar)

Q_i: Enthalpy of adsorption of component *i* (J/mol)

r_{Ni} and r_{YSZ}: Ni and YSZ radius (m)

R: Universal gas constant (8.314 J/mol.K)

RC: Reactant conversion

R_i: Ohmic resistance

R_{Y3+}: Ionic radius (Å)

T: Operating temperature (K)

t: Operating time (hr)

U: Operating voltage (V)

U_{EQ}: Equilibrium voltage (V)

U_P: Polarisation overpotential (V)

U_S: Ohmic overpotential (V)

V_{Ni}^c: Ni volume fraction at percolation

V_i: Volume fraction of component *i*

X_i: Weight fraction of component *i*

Y_i: Mole fraction of component *i*

Z: Average particle coordination number

$Z_{YSZ,YSZ}$: Coordination number between YSZ particles

Greek letters

α: Charge transfer coefficient

$\Delta G_{f,i}$: Gibbs free energy of formation for component *i* (J/mol)

ΔH: Enthalpy change of reaction (J/mol)

ΔS: Entropy change of reaction (J/mol)

ΔU: Degradation rate (%/1000hrs)

η_{syngas}: Syngas production efficiency (%)

θ_i: Surface coverage fraction of component *i*

λ: Electrolyte fitting parameter

ρ_i: Density of component *i* (g/cm^3)

σ_i^0: Pre-exponential factor for component *i* (S/cm)

σ_i: Conductivity of component *i* (S/cm)

τ: Time constant (hr)

Φ: Porosity

1. Introduction

1.1. Background

The abundant use of fossil fuels within the current global energy systems represents about 70% of CO_2 emissions which significantly contribute to global warming and climate change [1]. The Intergovernmental Panel on Climate Change (IPCC) recommends reducing CO_2 emissions to net-zero by 2050 [2]. One potential solution could be the deployment of synthetic fuels and chemicals. High-temperature SOECs are promising devices that use renewable electricity to convert H_2O to H_2 or CO_2 to CO through electrolysis. The unique feature of SOEC over other electrolyser devices is its ability to co-electrolyse CO_2 and H_2O to produce syngas ($CO+H_2$) which can be further converted into a wide range of chemicals and fuels via the FTS process [3,4].

By geometry, SOECs can be tubular or planar. By scale, single cells (Figure 1a) are assembled to make a stack as shown in Figure 1b (in the case of planar SOEC). Then, several stacks can be arranged to form a SOEC module [5]. Each single cell mostly consists of an anode or oxygen electrode, a cathode or fuel electrode and a dense electrolyte. Using an external power source, CO_2 and H_2O are co-reduced with electrons at the cathode electrode to produce CO and H_2 respectively (Reactions 1 and 2); both reactions also generate oxygen ions (O^{2-}) which are transported to the anode electrode through an ion-conducting membrane (electrolyte); oxygen ions combine to liberate oxygen (O_2) and electrons on the anode side (Reaction 3) [5,6].

$$CO_2 + 2e^- \rightarrow CO + O^{2-} \quad (1)$$

$$H_2O + 2e^- \rightarrow H_2 + O^{2-} \quad (2)$$

$$2O^{2-} \rightarrow O_2 + 2e^- \quad (3)$$

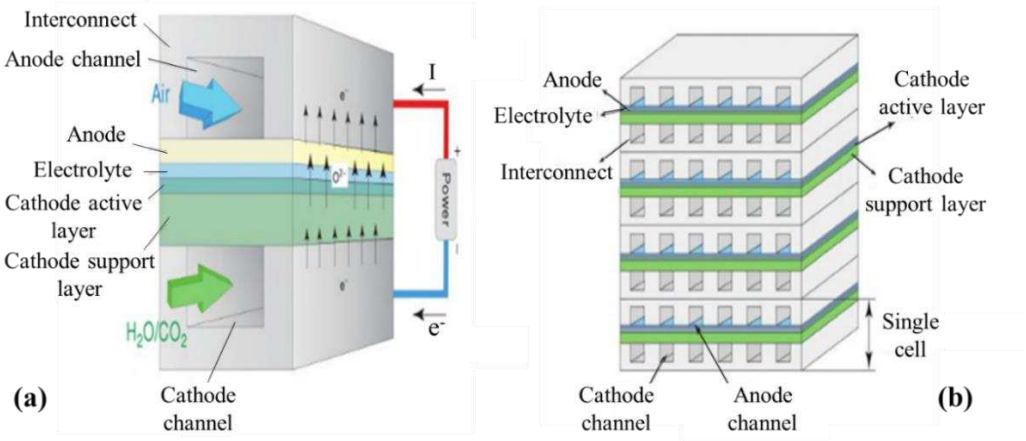

Figure 1: Schematic diagram of planar (a) single cell and (b) SOEC stack [6]

1.2. Previous studies

1.2.1. Studies on SOEC performance

One important parameter for SOEC is process performance. Several experimental studies have been carried out using 1-cell [4,7–11], 6-cell stack [12,13] and 10-cell stack [14–16] at temperatures between 700-900℃ and current densities up to 1.5 A/cm^2. Modelling and simulation approaches were also used to understand the physico-chemical phenomena occurring in SOEC and improve the process performance.

1.2.1.1. Steady-state modelling

Ni [17,18] developed 1D and 2D steady-state models of planar SOEC to study the electrochemical reactions and mass/heat transfer during CO_2/H_2O co-electrolysis. The models also included the reaction kinetics of methanation and RWGS to quantify their contributions during CO_2 and H_2O co-electrolysis. Xie and Xue [19] developed a 2D steady-state model of tubular SOEC in COMSOL MULTIPHYSICS®. They aimed to understand the surface co-electrolysis reactions and distribution of gas species within the electrodes based on mass, energy, momentum and charge balance. Stempien et al. [20] performed steady-state optimization of planar SOEC combined with power plant using macro-level modelling in Aspen HYSYS®. The authors assessed the effects of syngas recirculation, temperature and mole flux on SOEC performance and achieved 46.2% syngas efficiency at 1.54V and 800℃. Tubular and planar SOECs were investigated with micro 2D

modelling by Luo et al. [21] in COMSOL MULTIPHYSICS® and Menon et al. [22] in DETCHEM™, respectively. Luo et al. [21] studied the effects of operating conditions on SOEC performance and reported 59.4.% syngas efficiency at 1.4V and 700℃. Whereas, Menon et al. [22] analysed the effects of operating conditions and electrode microstructures on the species distribution. Hawkes et al. [23] developed a 3D steady-state model of planar SOEC using computational fluid dynamics (CFD) technique in FLUENT. Their results provided detailed profiles of operating voltage, temperature, current density and outlet gas composition for different operating conditions and achieved 55% syngas efficiency at 850℃.

1.2.1.2. Dynamic modelling

Dynamic modelling allows greater analysis of a process reaction to disturbances such as change of operation strategies and component failures. Zheng et al. [24] developed a 1D dynamic model of tubular SOEC to study the transient response of operation switching from SOEC to SOFC. The model considers electrochemical/chemical reactions, dynamics in mass and energy balance. They analysed transient responses of temperature, voltage, power density and syngas mole fraction during mode switching. Luo et al. [25] developed a micro 2D dynamic modelling of tubular SOEC in COMSOL MULTIPHYSICS® to assess the transient behaviour of CO_2/H_2O co-electrolysis when applying intermittent and unstable renewable energies. The model incorporates mass/heat transport, electrochemical/chemical reactions and momentum transfer. Dynamic process analysis was applied for optimal operation and achieved 66% syngas efficiency at 700℃ and 1.33V. Planar SOEC for large-scale applications was investigated by Banerjee et al. [26] with 3D dynamic modelling using CFD in DETCHEM™. The authors performed steady-state process optimisation and analysed transient responses during operation switching between electrolysis and co-electrolysis modes. A syngas efficiency of 68.5% was observed at 850℃ and 1.3V. For both steady-state and dynamic models aforementioned, only steady-state model validation was carried out by comparing voltage versus current density against experimental data.

1.2.2. Studies on SOEC degradation

Another important parameter for SOEC is durability. Degradation issue occurring inside SOECs is one of the main challenges that prevent their commercial deployment [5,27]. SOEC degradation is classified into three main categories including mechanical failure due to thermal stress, electrochemical/chemical degradation and structural degradation [28]. Structural degradation, resulting from the deterioration of SOEC components, represents one of the most critical degradations during SOEC long-term operation [5,28–30]. Most experimental studies have tested SOEC durability under co-electrolysis using Ni-YSZ/YSZ/LSM-YSZ (cathode/electrolyte/anode) cell configuration at 800-850°C and 0.25-1.5 A/cm^2 [4,8,31–33]. The authors reported tests below 1500 hours with up to 60% reactant conversion.

Modelling efforts were also devoted to clarify SOEC degradation mechanisms and improve the cell lifetime. Virkar [29] investigated the operating pressures leading to anode delamination using a 1D steady-state model based on charge transport. Chatzichristodoulou et al. [34] proposed a 2D steady-state model of planar SOEC based on mass transfer and charge transport to study the distribution of electrochemical and chemical overpotential across the electrolyte. A 2D steady-state model of tubular SOEC based on charge, momentum and energy conservation was developed by Nerat and Juričić [30] in COMSOL MULTIPHYSICS®. They aimed to assess the effect of anode delamination on the SOEC conversion efficiency. Navasa et al. [35] studied the temperature and overpotential distributions through the electrodes using a 3D steady-state model of planar SOEC in COMSOL MULTIPHYSICS®. Their model incorporates momentum/mass/heat transfer, electrochemical reactions and species transport to predict the spatial variations of gas composition, temperature and overpotential through the electrodes. The above-mentioned models for degradation were developed for SOEC under H_2O electrolysis. Wang et al. [36] investigated long-term operation strategies regarding degradation using a 2D steady-state model of planar SOEC under CO_2/H_2O co-electrolysis in Aspen Custom Modeler®. However, their study only looked at temperature management for a fixed degradation rate of 1.4 %/1000hrs. The authors observed that

increasing SOEC inlet temperature reduces the temperature gradient between the stack inlet and outlet hence limits thermal failures.

1.3. The aim and novelty of this paper

Most modelling studies on SOEC in the literature focused on performance only and did not consider cell degradation. Proposed models on degradation are mostly for SOEC during H_2O electrolysis whereas, information on SOEC degradation operating under CO_2/H_2O co-electrolysis remains scarce. Moreover, steady-state model validation (voltage versus current density) was performed for the aforementioned models on SOEC degradation. Understanding that SOEC degradation measures the increase of operating voltage with time at a specified current density [37], validation of adequate parameters is critical for SOEC degradation model establishment. To the best of our knowledge, no paper has been found in open literature presenting a SOEC model with structural degradation of cathode, electrolyte and anode materials. Although novel materials for SOEC are being explored, it is paramount to understand the factors causing the material structural damages with time to find effective strategies to reduce degradation and enhance SOEC lifetime.

This work aims to propose a 1D pseudo-dynamic model of planar SOEC running under CO_2/H_2O co-electrolysis. In comparison to Wang et al. [36], the model developed in this paper includes the material structural deterioration affecting the performance and degradation of a typical SOEC set: Ni-YSZ/YSZ/LSM-YSZ. The model is implemented in Aspen Plus® using Fortran® routines and validated for both performance (syngas outlet composition) and degradation (voltage versus time) for different current densities. Process analysis based on the developed model is then performed to assess the effects of operating conditions (current density, temperature, feed gas composition and flowrate) and structural degradation on SOEC long-term electrochemical performance, durability and syngas production.

2. Model development

To develop the 1D pseudo-dynamic model for planar SOEC, the following were considered:

- The model consists of two sub-models: (1) model for the equilibrium voltage and (2) model for the overpotentials resulting from structural degradation of SOEC component materials.
- Although the model parameters of the equilibrium voltage are generic for all SOECs, the governing equations for the structural degradation are specific to the chosen SOEC material set. This is because degradation mechanisms are different for each material composition.
- The sum of the equilibrium voltage and overpotentials represents the SOEC operating voltage.
- Only the structural degradation of SOEC component materials is considered dynamically i.e. mass or heat accumulation inside the cell is ignored.

2.1. Equilibrium voltage

The equilibrium or open cell voltage (U_{EQ}) represents the minimum electrical voltage required for the electrolysis reactions to occur [28]. Since more than one electrochemical reaction occurs at the TPB, the mixed theory potential is used to evaluate the equilibrium voltage. It represents the superposition of potentials resulting from CO_2 and H_2O co-electrolysis (Equation 4). Assuming the adsorption of gas molecules on the electrode surface follows the Langmuir isotherm and empty sites do not influence the equilibrium voltage, Θ_i is calculated based on the modified Langmuir adsorption law as described by Equations 5 and 6 [3,28].

$$U_{EQ} = \Theta_{CO_2}\left|-\frac{\Delta G_{f,CO_2}}{nF} - \frac{RT}{nF} ln\left[\frac{Y_{CO_2}}{Y_{CO}\, Y_{O_2}^{0.5}}\left(\frac{P}{P_{std}}\right)^{-0.5}\right]\right| + \Theta_{H_2O}\left|-\frac{\Delta G_{f,H_2O}}{nF} - \frac{RT}{nF} ln\left[\frac{Y_{H_2O}}{Y_{H_2}\, Y_{O_2}^{0.5}}\left(\frac{P}{P_{std}}\right)^{-0.5}\right]\right| \quad (4)$$

$$\Theta_i = \frac{K_i \times Y_i}{\sum_j K_j Y_j} \quad (5)$$

$$K_i = K_i^0 exp\left(\frac{Q_i}{RT}\right) \quad (6)$$

The mole fractions of products and reactants at the electrode-electrolyte interface are included in Equation 4. Hence, concentration overpotentials are implicitly included in the equilibrium voltage [17].

2.2. Ni-YSZ cathode degradation

Ni-YSZ degradation is mostly caused by the growth of Ni particles at high temperatures via sintering. The increase of particle size in the YSZ phase reduces both the electronic conductivity within Ni phase and the TBP length [38]. Assuming Ni agglomeration takes place via Ni_2-OH formation in the presence of H_2O, the evolution of Ni particle size with time is described by Equation 7 as follows [39,40]:

$$\frac{d(r_{Ni})}{dt} = C\frac{X_{Ni}}{X_{YSZ}\times A_{YSZ}\times r_{Ni}^6}\left(\frac{Y_{H_2O}}{Y_{H_2}^{0.5}}\right)exp\left(-\frac{E_{sin}}{RT}\right) \quad (7)$$

Equation 7 is integrated and Ni radius is derived as shown in Equation 8.

$$r_{Ni} = \left|r_{Ni,0}^7 + C\frac{X_{Ni}\times t}{X_{YSZ}\times A_{YSZ}}\left(\frac{Y_{H_2O}}{Y_{H_2}^{0.5}}\right)exp\left(-\frac{E_{sin}}{RT}\right)\right|^{1/7} \quad (8)$$

Equations 9 and 10 describe the initial and after time t of the TPB length and volume for Ni particles in terms of particle number N (assuming the cathode is a system with random packing of spherical particles) [38].

$$L_{TPB} = 2\pi \times N \times r_{Ni};\ L_{TPB,0} = 2\pi \times N_0 \times r_{Ni,0} \quad (9)$$

$$V = \frac{4}{3}\pi \times N \times r_{Ni}^3;\ \ V_0 = \frac{4}{3}\pi \times N_0 \times r_{Ni,0}^3 \quad (10)$$

Mass balance of Ni particles at constant density requires V_0=V.

$$\text{Therefore, } V = V_0 \Rightarrow N \times r_{Ni}^3 = N_0 \times r_{Ni,0}^3 \quad (11)$$

Combining Equations 9 and 11 gives Equation 12. The TPB length change due to Ni particle growth is then expressed as shown in Equation 13.

$$L_{TPB} \times r_{Ni}^2 = L_{TPB,0} \times r_{Ni,0}^2 \quad (12)$$

$$\frac{L_{TPB}}{L_{TPB,0}} = \frac{r_{Ni,0}^2}{r_{Ni}^2} \quad (13)$$

The high field approximation of the Butler-Volmer equation (Equation 14) relates the polarisation voltage with current density [38]. Equation 14 is re-written as Equation 15, which gives Equation 16 after time differentiation. Here, the subscript *i* represents the cathode or anode.

$$j = j_0 exp\left(\frac{\alpha \times n \times F}{RT} U_{P,i}\right) \quad (14)$$

$$\frac{j}{j_0} = exp\left(\frac{\alpha \times n \times F}{RT} U_{P,i}\right) \Rightarrow ln\left(\frac{j}{j_0}\right) = \frac{\alpha \times n \times F}{RT} U_{P,i} \quad (15)$$

$$dln\left(\frac{j}{j_0}\right) = \frac{\alpha \times n \times F}{RT} dU_{P,i} = \frac{\alpha \times n \times F}{RT}\left(\frac{dU_{P,i}}{dt}\right) dt \quad (16)$$

Integration of Equation 16 gives Equation 17. Considering that $U_{P,i}(0) = 0$ and the exchange current density is proportional to the TPB length [38], Equation 18 describes the polarisation voltage in terms of TBP length.

$$ln(j) - ln\left(\frac{j_0}{j_{0,0}}\right) = \frac{\alpha \times n \times F}{RT}\left[U_{P,i}(t) - U_{P,i}(0)\right] \quad (17)$$

$$U_{P,i}(t) = \frac{RT}{\alpha \times n \times F}\left[ln(j) - ln\left(\frac{L_{TPB}}{L_{TPB,0}}\right)\right] \quad (18)$$

The combination of Equations 13 and 18 gives the polarisation voltage at the cathode as expressed in Equation 19.

$$U_{P,Cat}(t) = \frac{RT}{\alpha \times n \times F}\left[ln(j) - ln\left(\frac{r_{Ni,0}^2}{r_{Ni}^2}\right)\right] \quad (19)$$

The electronic conductivity of Ni-YSZ composite is calculated using Equation 20. Since σ_{YSZ} is very low compared to σ_{Ni}, σ_{YSZ} (hence, the second term in Equation 20) is assumed negligible [41].

$$\sigma_{Ni-YSZ} = V_{Ni}\sigma_{Ni} + V_{YSZ}\sigma_{YSZ} \quad (20)$$

The time evolution of Ni effective conductivity is evaluated based on the percolation theory as following [42,43]:

$$\sigma_{Ni} = \sigma_{Ni,0}\left(\frac{V_{Ni} - V_{Ni}^c}{1 - {}^{\Phi}/_{(1+\Phi)} - V_{Ni}^c}\right)^2 \quad (21)$$

$$\sigma_{Ni,0} = 3.27 \times 10^4 - 10.65 \times T \quad (22)$$

$$Z \frac{{}^{V_{Ni}^c}/_{r_{Ni}}}{{}^{V_{Ni}^c}/_{r_{Ni}} + {}^{(1-V_{Ni}^c)}/_{r_{YSZ}}} = 1.764 \quad (23)$$

$$Z = Z_{YSZ,YSZ} \frac{{}^{V_{Ni}}/_{r_{Ni}} + {}^{V_{YSZ}}/_{r_{YSZ}}}{{}^{V_{YSZ}}/_{r_{YSZ}}} \quad (24)$$

YSZ particle size is assumed to remain the same due to their high melting temperatures [38]. Therefore, $r_{YSZ} = r_{YSZ,0}$. The ohmic overpotential on the cathode side is determined according to Ohm's law as follows:

$$U_{S,Cat}(t) = \frac{d_{Ni-YSZ}}{\sigma_{Ni-YSZ}} \times j \quad (25)$$

2.3. YSZ electrolyte degradation

Under reducing environment and high temperatures, there is a phase transformation of YSZ crystal structure from cubic to tetragonal phase due to cation diffusion, which leads to loss of YSZ ionic conductivity [44]. According to Ohm's law, the decrease in electrolyte conductivity with time increases the ohmic voltage (Equation 26). The time dependence of YSZ conductivity is calculated using Equation 27, wherein the time constant τ indicates YSZ structure stability and depends on the dopant radius as shown in Equation 29 [45].

$$U_{S,El}(t) = \frac{d_{El}}{\sigma_{El}} \times j \quad (26)$$

$$\sigma_{El} = \sigma_{El,0} \left[\lambda + (1-\lambda) exp\left(-\frac{t}{\tau}\right)\right] \quad (27)$$

$$\sigma_{El,0} = \frac{\sigma_{El}^0}{T} exp\left(-\frac{E_{a,El}}{RT}\right) \quad (28)$$

$$\tau = 7.23 \times 10^{-38} exp\,(89.8 \times r_{Y^{3+}}) \quad (29)$$

2.4. LSM-YSZ anode degradation

There are three main structural degradations responsible for LSM-YSZ anode delamination including lanthanum zirconate formation, Cr contamination and LSM-YSZ particle coarsening [28,46].

2.4.1. Formation of lanthanum zirconate

At the YSZ electrolyte boundaries and LSM-YSZ interface, O^{2-} ions are oxidized to O_2 (Reaction 3) creating high P_{O_2} near the LSM-YSZ interface. High P_{O_2} favours $La_2Zr_2O_7$ (LZO) formation from $LaMnO_3$ of LSM and ZrO_2 of YSZ (Reaction 30). The accumulation of LZO causes an increase in ohmic resistance on the anode side due to LZO poor conductive properties [47].

$$LaMnO_3 + ZrO_2 + 0.25O_2 \rightleftharpoons 0.5La_2Zr_2O_7 + MnO_2 \quad (30)$$

LZO formation takes place via Mn^{2+} diffusion from LSM to YSZ and subsequent Zr^{4+} and La^{3+} diffusion towards the anode-electrolyte interface [48]. Therefore, LZO layer thickness growth with time is calculated based on Wagner's law for parabolic oxidation as described by Equations 31 and 32. Equations 33 and 34 evaluate the ohmic resistance due to LZO growth.

$$d_{LZO}^2(t) = \left(K_{P,LZO} \times t\right) exp\left(-\frac{E_{LZO}}{RT}\right) \quad (31)$$

$$K_{P,LZO} = \frac{K_{g,LZO}}{\left(X_{O,LZO} \times \rho_{LZO}\right)^2} \quad (32)$$

$$R_{LZO} = \frac{d_{LZO}(t)}{\sigma_{LZO}} \quad (33)$$

$$\sigma_{LZO} = \frac{\sigma_{LZO}^0}{T} exp\left(-\frac{E_{a,LZO}}{RT}\right) \quad (34)$$

2.4.2. Cr contamination

To build a SOEC stack, each single cell requires an interconnect to connect the anode of one cell to the cathode of the adjoining cell. Fe-Cr alloys (such as Haynes 230 and Crofer 22APU) are often preferred as interconnect materials due to their good electrical conductivity, easy availability and low cost [49]. However, under high temperatures, Cr compounds are oxidized by gaseous O_2 to

form a chromium oxide scale (Reaction 35) at the interface between the interconnect and the anode [49,50].

$$2Cr^0 + 1.5O_2 \rightleftharpoons Cr_2O_{3(s)} \quad (35)$$

Assuming Cr_2O_3 is the only chromium oxide scale (COS) layer formed and its formation takes place via Cr^{3+} and O^{2-} diffusion, COS thickness evolution with time is also evaluated using Wagner's law for parabolic oxidation (Equation 36) [50]. Equations 37–39 describe the ohmic overpotential on the anode side due to LZO and COS growth.

$$d_{COS}^2(t) = \frac{K_{g,COS} \times t}{(X_{O,COS} \times \rho_{COS})^2} exp\left(-\frac{E_{COS}}{RT}\right) \quad (36)$$

$$U_{S,An}(t) = (R_{LZO} + R_{COS}) \times j \quad (37)$$

$$R_{COS} = \frac{d_{COS}(t)}{\sigma_{COS}} \quad (38)$$

$$\sigma_{COS} = \frac{\sigma_{COS}^0}{T} exp\left(-\frac{E_{a,COS}}{RT}\right) \quad (39)$$

2.4.3. LSM-YSZ phase coarsening

Under high temperatures, the anode microstructures (especially near electrolyte/anode interface) become coarser and denser leading to a decrease in the TBP length on the anode side [51]. The model for LSM-YSZ degradation due to particle coarsening is based on the following:

- Since YSZ coarsening is very slow [51], LSM-YSZ degradation is only due to LSM phase coarsening.
- LSM phase coarsening is due to Mn^{2+} particles diffusion on the LSM surface towards LSM-YSZ interface to reach TBP active sites [46,51].

The mass transport of diffused particles in one dimension is described using Fick's second law (Equation 40) in which the TBP length represents the concentration of diffused particles. The solution to the Fick's law equation is given by Equation 41 when the surface concentration is zero (i.e. $x = 0$ and $L_{TPB} = L_{TPB,0}$) [46,52]. Integrating Equation 41 gives Equation 43 which describes the variation of TPB length with time.

$$\frac{\partial}{\partial t} L_{TPB} = D_{LSM} \frac{\partial^2}{\partial x^2} L_{TPB} \quad (40)$$

$$\left(D_{LSM} \frac{d}{dx} L_{TPB} \right)_{x=0} = \frac{L_{TPB,0} \times D_{LSM}}{\sqrt{\pi t \times D_{LSM}}} \quad (41)$$

$$\frac{L_{TPB}}{L_{TPB,0}} = 1 - 2 \times \left(\frac{t \times D_{LSM}}{\pi} \right)^{1/2} \quad (42)$$

The polarisation voltage at the anode is obtained by combining Equations 18 and 42 as shown in Equation 43.

$$U_{P,An}(t) = \frac{RT}{\alpha \times n \times F} \left[ln(j) - ln \left| 1 - 2 \times \left(\frac{t \times D_{LSM}}{\pi} \right)^{1/2} \right| \right] \quad (43)$$

3. Simulation

All the calculations were carried out using Aspen Plus® software. Since SOEC is not a standard component in Aspen Plus® Library, SOEC unit was simulated combining basic Aspen Plus® blocks and Fortran® routines for the structural degradation model implementation. Table 1 recapitulates the equations implemented in Aspen Plus®. The property method used for the simulation is Peng-Robison. This is because Peng-Robison gives more reliable results for non-polar compounds such as CO_2, CH_4 and H_2. Figure 2 illustrates the SOEC unit flowsheet developed in this work.

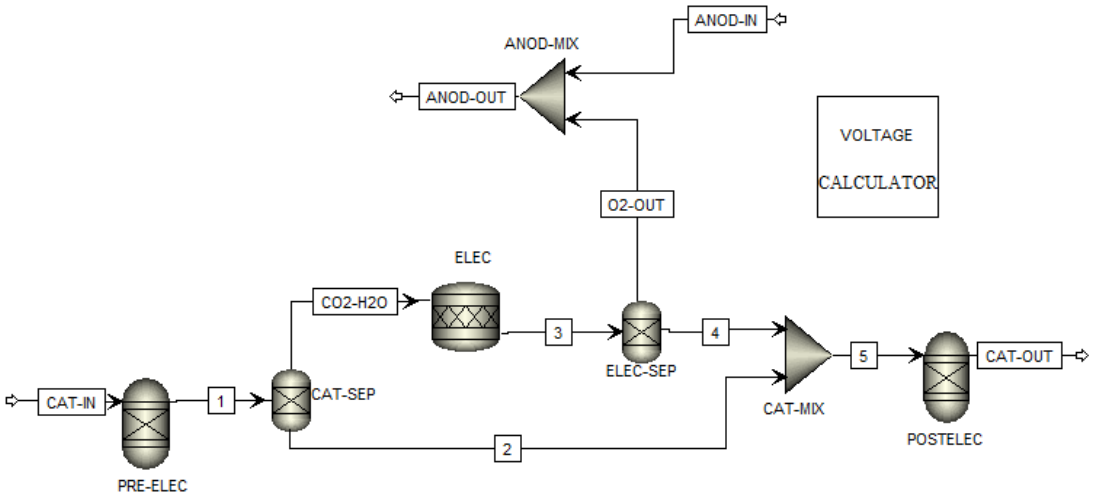

Figure 2: Process flowsheet of SOEC unit in Aspen Plus®

Table 1: Summary of mathematical modelling

Parameter	Equation
Adsorption constant (Equation 6)	$K_i = K_i^0 exp\left(\frac{Q_i}{RT}\right)$
Surface coverage fraction (Equation 5)	$\Theta_i = \frac{K_i \times Y_i}{\sum_j K_j Y_j}$
Equilibrium voltage (Equation 4)	$U_{EQ} = \Theta_{CO_2}\left\|-\frac{\Delta G_{f,CO_2}}{nF} - \frac{RT}{nF} ln\left[\frac{Y_{CO_2}}{Y_{CO}\, Y_{O_2}^{0.5}}\left(\frac{P}{P_{std}}\right)^{-0.5}\right]\right\| + \Theta_{H_2O}\left\|-\frac{\Delta G_{f,H_2O}}{nF} - \frac{RT}{nF} ln\left[\frac{Y_{H_2O}}{Y_{H_2}\, Y_{O_2}^{0.5}}\left(\frac{P}{P_{std}}\right)^{-0.5}\right]\right\|$
Ni radius (Equation 8)	$r_{Ni} = \left\|r_{Ni,0}^7 + C\frac{X_{Ni} \times t}{X_{YSZ} \times A_{YSZ}}\left(\frac{Y_{H_2O}}{Y_{H_2}^{0.5}}\right) exp\left(-\frac{E_{sin}}{RT}\right)\right\|^{1/7}$
Polarisation voltage at the cathode (Equation 19)	$U_{P,Cat}(t) = \frac{RT}{\alpha \times n \times F}\left[ln(j) - ln\left(\frac{r_{Ni,0}^2}{r_{Ni}^2}\right)\right]$
Intrinsic Ni conductivity (Equation 22)	$\sigma_{Ni,0} = 3.27 \times 10^4 - 10.65 \times T$
Average coordination number (Equation 24)	$Z = Z_{YSZ,YSZ}\frac{V_{Ni}/r_{Ni} + V_{YSZ}/r_{YSZ}}{V_{YSZ}/r_{YSZ}}$
Ni volume fraction at percolation (Equation 23)	$Z\frac{V_{Ni}^c/r_{Ni}}{V_{Ni}^c/r_{Ni} + (1 - V_{Ni}^c)/r_{YSZ}} = 1.764$
Ni effective conductivity (Equation 21)	$\sigma_{Ni} = \sigma_{Ni,0}\left(\frac{V_{Ni} - V_{Ni}^c}{1 - \Phi/(1 + \Phi) - V_{Ni}^c}\right)^2$
Ni-YSZ conductivity (Equation 20)	$\sigma_{Ni-YSZ} = V_{Ni}\sigma_{Ni}$
Ohmic voltage at the cathode (Equation 25)	$U_{S,Cat}(t) = \frac{d_{Ni-YSZ}}{\sigma_{Ni-YSZ}} \times j$

Time constant (Equation 29)	$\tau = 7.23 \times 10^{-38} exp\ (89.8 \times r_{Y^{3+}})$
Intrinsic YSZ conductivity (Equation 28)	$\sigma_{El,0} = \frac{\sigma_{El}^{0}}{T} exp\left(-\frac{E_{a,El}}{RT}\right)$
YSZ ionic conductivity (Equation 27)	$\sigma_{El} = \sigma_{El,0}\left[\lambda + (1-\lambda) exp\left(-\frac{t}{\tau}\right)\right]$
Ohmic voltage at the electrode (Equation 26)	$U_{S,El}(t) = \frac{d_{El}}{\sigma_{El}} \times j$
LZO conductivitity (Equation 34)	$\sigma_{LZO} = \frac{\sigma_{LZO}^{0}}{T} exp\left(-\frac{E_{a,LZO}}{RT}\right)$
COS conductivitity (Equation 39)	$\sigma_{COS} = \frac{\sigma_{COS}^{0}}{T} exp\left(-\frac{E_{a,COS}}{RT}\right)$
LZO layer thickness (Equation 31)	$d_{LZO}^{2}(t) = \frac{K_{g,LZO} \times t}{\left(X_{O,LZO} \times \rho_{LZO}\right)^{2}} exp\left(-\frac{E_{LZO}}{RT}\right)$
COS layer thickness (Equation 36)	$d_{COS}^{2}(t) = \frac{K_{g,COS} \times t}{\left(X_{O,COS} \times \rho_{COS}\right)^{2}} exp\left(-\frac{E_{COS}}{RT}\right)$
Ohmic voltage at the anode (Equation 37)	$U_{S,An}(t) = \left(\frac{d_{LZO}(t)}{\sigma_{LZO}} + \frac{d_{COS}(t)}{\sigma_{COS}}\right) \times j$
Polarisation voltage at the anode (Equation 43)	$U_{P,An}(t) = \frac{RT}{\alpha \times n \times F}\left[ln(j) - ln\left\lvert 1 - 2 \times \left(\frac{t \times D_{LSM}}{\pi}\right)^{1/2}\right\rvert\right]$

The feed gas enters a Gibbs reactor (PRE-ELEC) and reaches equilibrium based on the RWGS reaction (Reaction 44). Reactants (CO_2-H_2O) are separated from other gases and sent to a Stoic reactor (ELEC) where they are co-electrolysed following Reactions 1 and 2. The reactant conversion (RC) fraction is evaluated based on Faraday's law as described by Equation 45. In reality, O_2 and syngas are produced in different compartments. Hence, a separator unit (ELEC-SEP) is added to remove O_2 from other gases. All cathodic flows are mixed and sent to another

Gibbs reactor (POSTELEC) where both RWGS and steam reforming/methanation (Reaction 46) reactions occur. The hypothesis of equilibrium reactions 44 and 46 occurring before and after co-electrolysis reactions is based on kinetic values at high temperatures and in the presence of Ni catalyst [14,53].

$$CO_2 + H_2 \rightleftharpoons CO + H_2O \quad (44)$$

$$RC = \frac{I}{n \times F \times \dot{N}_{in}} = \frac{A_{cell} \times N_{cell} \times j}{n \times F \times \dot{N}_{in}} \quad (45)$$

$$CH_4 + H_2O \rightleftharpoons CO + 3H_2 \quad (46)$$

4. Model validation

SOEC model was validated using experimental data from the literature. Two sets of data were selected to numerically validate SOEC performance and structural degradation. In this section, each single cell is made of Ni-8YSZ/8YSZ/$(La_{0.75}Sr_{0.25})_{0.95}MnO_3$-8YSZ and Crofer 22 APU interconnect wherein 8 indicates Y_2O_3 mol% in YSZ. During experiments, H_2 is added to the cathode feed gas to avoid Ni oxidation and Air/O_2 is continuously supplied to the anode to prevent LSM-YSZ change of state [8,53].

4.1. Validation of SOEC performance

Experiments from FuelCell Lab at the University of Perugia [53] were used to validate SOEC performance. SOEC stack consists of four planar cells supplied by Forschungszentrum Jülich. Three experimental tests were performed to assess SOEC performance in CO_2/H_2O co-electrolysis mode. SOEC details and test parameters are provided in Table 1. Validation results are presented in terms of CO_2, H_2 and CO outlet mole fractions as a function of current density (Figure 3). The results were obtained by simulating SOEC model under the operating conditions given in Table 1.

Table 1: SOEC characteristics and test parameters from FuelCell Lab [53]

Parameter	Test 1	Test 2	Test 3
Cathode feed composition: $CO_2/H_2O/H_2$ (%mol)	20/70/10	30/60/10	40/50/10
Cathode flowrate (mol/hr)	8.53		
Cathode thickness (µm)	7 – 10		
Anode flowrate (mol/hr)	8.92		
Anode thickness (µm)	10 – 15		
Electrolyte thickness (µm)	8 – 10		
Operating temperature (°C)	750		
Operating pressure (bar)	1.0		
Cell size (cm^2)	10 × 10		
Active cell area (cm^2)	80		
Number of cells	4		

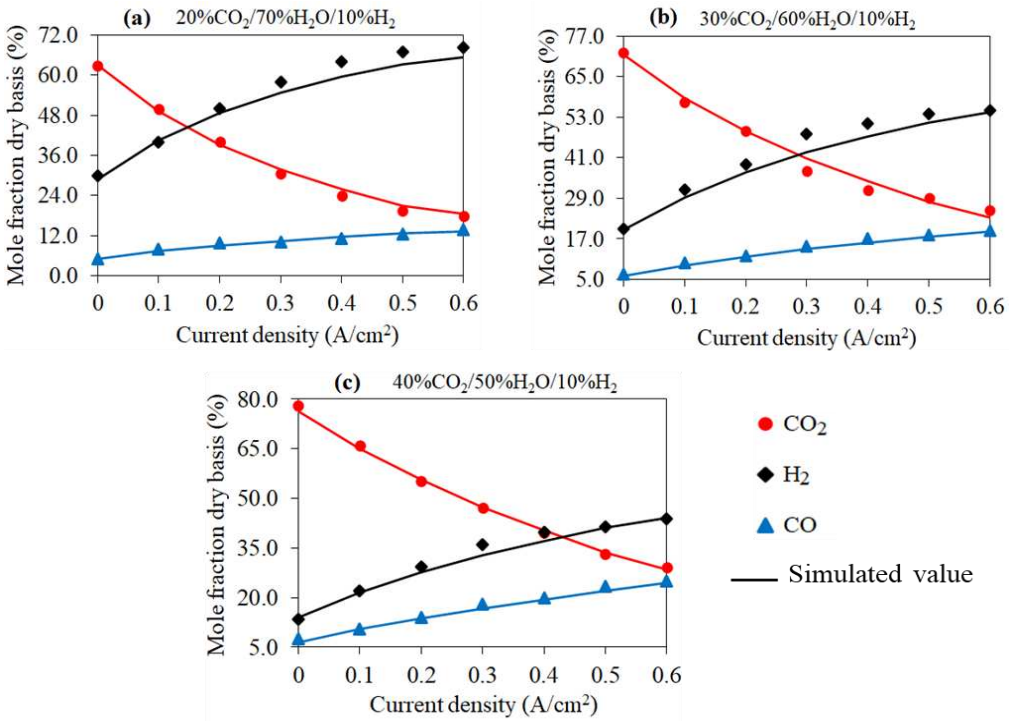

Figure 3: Experimental values of outlet syngas composition (symbols) compared to model predictions (solid lines) for different inlet feed compositions

Table 2: Highest relative errors observed during SOEC performance validation

Current density (A/cm^2)	Relative errors (%)		
	Test 1	Test 2	Test 3
0.0	4.0	7.7	13.2
0.1	8.8	9.0	3.2
0.2	7.1	6.2	5.1
0.3	5.5	11.5	8.9
0.4	7.9	7.5	6.3
0.5	7.2	4.8	5.5
0.6	4.3	8.6	2.6

Despite some discrepancies (Table 2), SOEC model gives fairly good predictions of syngas composition profiles. These discrepancies might be because the outlet syngas composition is experimentally obtained using gas chromatography which requires a dry sample (i.e. H_2O mol% = 0). However, during simulations, even after condensing water out from syngas, there is still some H_2O fraction (~2.9%) remaining in the produced gas which may affect the outlet composition obtained from the simulation.

4.2. Validation of SOEC degradation

To validate the pseudo-dynamic model for SOEC structural degradation, data from experiments carried out at DTU Energy Conversion (former Risø DTU) [8,32] were used. The test rigs were 10-cell and 2-cell planar stacks produced at Risø DTU in Denmark. Two experiments were carried out to investigate SOEC durability under co-electrolysis at low and high current densities. During Test 1, the 10-cell SOEC stack was first operated at a current density of 0.5 A/cm^2 for 800 hours then, at 0.75 A/cm^2 for another 350 hours. At the current density of 0.75 A/cm^2, the cathode feed flowrate was increased from 360 to 540 L/hr to maintain a reactant conversion of 60%. Test 2 was carried

out using the 2-cell SOEC stack at a current density of 1.0 A/cm^2 for roughly 1000 hours. The experimental conditions and SOEC characteristics are presented in Table 3.

Table 3: SOEC characteristics and test parameters from DTU Energy Conversion [8,32]

Parameter	Test 1	Test 2
Cathode feed composition: $CO_2/H_2O/H_2$ (%mol)	45/45/10	45/45/10
Cathode flowrate (L/hr)	360/540	25
Cathode thickness (µm)	10	10
Cathode porosity (%)	40	40
Volume Fraction (Ni/YSZ)	40/60	40/60
Initial Ni radius (µm)	4.5	4.5
Initial YSZ radius (µm)	4	4
YSZ surface area (m^2/g)	0.41	0.41
Anode feed composition: O_2 (%mol)	100	100
Anode flowrate (L/hr)	60	50
Anode thickness (µm)	20	20
Anode porosity (%)	35	35
Volume Fraction (LSM/YSZ)	50/50	50/50
Electrolyte thickness (µm)	12	12
Operating temperature (°C)	850	800
Operating pressure (bar)	1.0	1.0
Cell size (cm^2)	12 × 12	5 × 5
Active cell area (cm^2)	92.16	16
Number of cells	10	2

Table 4: Properties used for SOEC pseudo-dynamic model validation.

Parameter	Value	Reference
H_2O adsorption constant	9.25	[3]
CO_2 adsorption constant	2.27	
H_2O enthalpy of adsorption (J/mol)	13200	
CO_2 enthalpy of adsorption (J/mol)	18,828	
Activation energy for sintering (J/mol)	332,000	[54]
YSZ coordination number	6	[43]
Electrolyte activation energy (J/mol)	80,000	[22]
Electrolyte pre-exponential factor (S/cm)	360,000	
Ionic radius (Å)	1.01	[45]
LSM surface diffusion (cm^2/hr)	1.12×10^{-5}	[46]
LZO density (g/cm^3)	6.05	[55]
Weight gain rate for LZO growth (g^2/cm^4.hr)	4.43×10^{-2}	
Activation energy for LZO growth (J/mol)	206,273	
LZO activation energy (J/mol)	55,000	
LZO pre-exponential factor (S/cm)	225.49	
COS density (g/cm^3)	5.255	[49,50]
Weight gain rate for COS growth: Test 1/Test 2 (g^2/cm^4.hr)	6.84×10^{-10} / 2.40×10^{-09}	
Activation energy for COS growth (J/mol)	220,000	
COS activation energy (J/mol)	86,200	
COS pre-exponential factor (S/cm)	320,000	

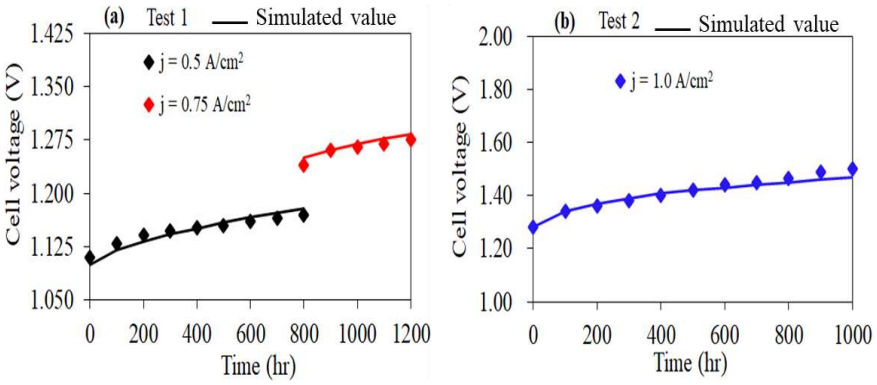

Figure 4: Experimental values of SOEC degradation (symbols) compared to model predictions (solid lines) for different current densities

Table 5: Comparison of cell degradation between experimental data from Risø DTU and model predictions

Time (hr)	Data from DTU (V)	Aspen Plus® simulation (V)	Relative error (%)
0	1.11	1.10	0.90
200	1.14	1.13	0.79
400	1.15	1.15	0.17
600	1.16	1.17	0.52
800	1.24	1.25	0.81
1,000	1.26	1.27	0.40
1,200	1.27	1.28	0.63

The results presented in this section were obtained by simulating the pseudo-dynamic model for planar SOEC under the conditions given in Table 3. Due to the unavailability of all required data, some parameters (Table 4) were assumed within realistic ranges based on available literature. Figures 4a and 4b portray good agreement between the model predictions and experimental data with relative errors below 1.0% as observed in Table 5. These results show that the pseudo-dynamic model developed in Aspen Plus® using Fortran® routines is able to reasonably predict both SOEC structural degradation and syngas composition at different input conditions. Therefore, the model can be used for further parametric analysis.

5. Process analysis

In this section, the pseudo-dynamic model developed and validated is used to predict SOEC long-term electrochemical performance and syngas production. Process analysis is carried out for 20,000 hours of operation which represents the minimum desired lifetime for SOEC stacks [37]. Equations 47 and 48 are used to evaluate the average SOEC degradation rate and syngas production efficiency, respectively [56]. It is important to specify that extended analysis might also include further external factors such as heat duty of heaters and network of pumps and compressors for reactant pre-treatment before entering SOEC. In this work, pre-treatment of reactants is neglected and we assumed 10% losses to the SOEC system.

$$\Delta U = \frac{U(t)-U(t_0)}{U(t_0)\times(t-t_0)} \times 100\% \qquad (47)$$

$$\eta_{syngas} = \frac{HHV_{out}}{HHV_{in}+P_{cell}} \qquad (48)$$

$$P_{cell} = U(t) \times j \times A_{cell} \qquad (49)$$

5.1. Effect of current density on degradation and syngas efficiency

5.1.1. Justification for case study

Current density is an important parameter to achieve high reactant conversion and syngas production. A good understanding of its effect on SOEC long-term performance is needed to evaluate the current density that gives the best production rate with minimum degradation.

5.1.2. Setup of the case study

To implement this case study, 800℃, 45%CO_2/45%H_2O/10%H_2 feed gas and 360 L/hr cathode flowrate were used. SOEC characteristics are as shown in Tables 3 and 4. The current density was varied from 0.5 to 1.5 A/cm^2.

5.1.3. Results and discussion

Figure 5 shows the effect of current density on SOEC operating voltage and syngas production efficiency. After 20,000 hours of operation, syngas production efficiency decreases from 56.5 to

48.6% at 0.5 A/cm^2, 53.5 to 41.3% at 1.0 A/cm^2 and 51.7 to 36.4% at 1.5 A/cm^2 with an average voltage degradation rate of 1.89, 3.27 and 4.47%/1000hrs, respectively. Increasing the current density results in higher reactant conversion (Equation 45) which subsequently leads to more CO and H_2 being generated (Figure 3). However, the operating voltage increases faster at higher current densities leading to lower syngas production due to high power utilisation. This agrees with experimental findings which showed that ohmic and polarisation voltages are more pronounced at higher current densities [4,8]. Therefore, SOEC performance and durability needs to be improved at high current densities.

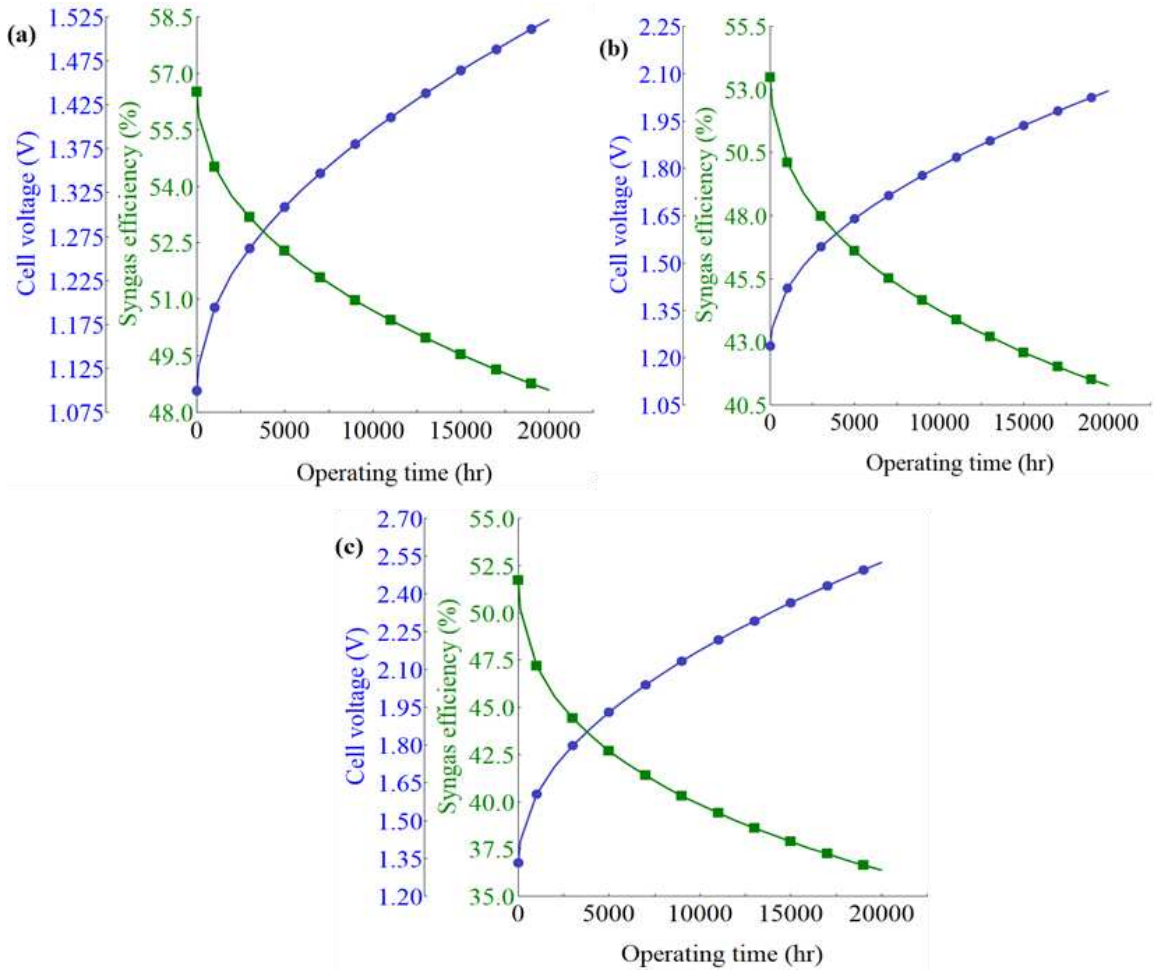

Figure 5: Evolution of SOEC voltage and syngas production efficiency with operating time for (a) j = 0.5 A/cm^2, (b) j = 1.0 A/cm^2 and (c) j = 1.5 A/cm^2

5.2. Effect of temperature on degradation and syngas efficiency

5.2.1. Justification for case study

Temperature is a key parameter for adsorption, electrochemical/chemical reaction and mass transfer within SOEC [5]. As a result, it is important to understand the relationship between temperature and SOEC long-term performance.

5.2.2. Setup of the case study

To carry out this case study, SOEC temperature was varied from 750 to 850℃ at two current densities, 1.0 and 1.5 A/cm^2. This is needed to assess the impact of lower and higher temperatures at high current densities. The remaining operating conditions are the same as Section 5.2.1.

5.2.3. Results and discussion

The results show that the equilibrium voltage decreases with rising temperatures at both 1.0 and 1.5 A/cm^2 current densities (Figure 6a). This is because the thermal energy increases with temperatures resulting in lower Gibbs free energy (Equation 50) [5] hence, lower equilibrium voltage. Higher temperatures also enhance electrochemical reactions leading to increased reactant conversion and syngas production [22]. This explains the increase in initial syngas production efficiency with temperature (Figure 6b).

$$\Delta G = \Delta H - (T \times \Delta S) \qquad (50)$$

Figures 6a and 6b also show that the required voltage and syngas production efficiency respectively increases and decreases faster at higher temperatures with operating time. For instance, at 1.0 A/cm^2, syngas efficiency lowers from 53.0 to 43.0% at 750℃ and 54.0 to 39.4% at 850℃. The average SOEC degradation rates are 2.56 and 4.10%/1000hrs at 750℃ and at 850℃, respectively. This is due to the direct dependence of structural degradation including Ni agglomeration (Equation 8), LZO (Equation 31) and chromium oxide (Equation 36) layer formation on the operating temperature. These chemical reactions are enhanced with rising temperatures leading to higher

degradation rates and lower production efficiency. Therefore, lowering SOEC operating temperature seems more beneficial regarding long-term performance.

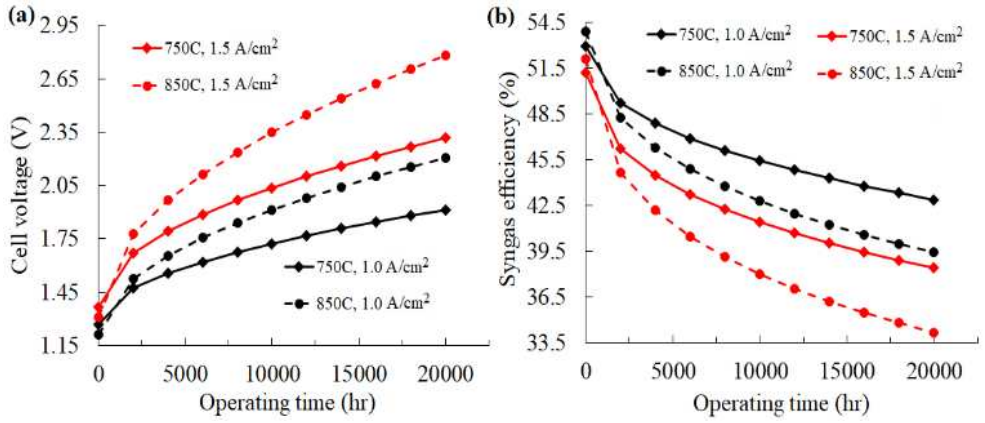

Figure 6: Evolution of (a) SOEC voltage and (b) syngas production efficiency for different operating temperatures

5.3. Effect of feed gas composition and flowrate on degradation and syngas efficiency

5.3.1. Justification for case study

Feed gas composition and flowrate are important parameters for the syngas quality (H_2/CO). Achieving the desired H_2/CO (~1.8 to 2.1) ratio is essential for FTS process [9]. It is, therefore, necessary to investigate the syngas quality (hence, feed gas composition and flowrate) profile during SOEC long-term performance.

5.3.2. Setup of the case study

To implement the case study, 750℃ and 1.0 A/cm^2 were used. Two scenarios were considered for the feed composition, S1: 30%CO_2/60%H_2O/10%H_2 and S2: 60%CO_2/30%H_2O/10%H_2 (in mol%) using 360 L/hr flowrate. To study the effect of flowrate, its value was varied from 290 to 420 L/hr using 30%CO_2/60%H_2O/10%H_2 feed gas. The remaining process conditions are shown in Tables 3 and 4.

5.3.3. Results and discussion

Figure 7a and Table 6 depicts the effect of cathode feed composition on SOEC long-term performance. Higher H_2O mole fraction lowers the required voltage and also improves the syngas quality (H_2/CO_{out}) during operation. The voltage rises with CO_2 feed fraction due to an increase of

concentration overpotentials arising from the slower CO_2 diffusion kinetics compared to H_2O [4]. The syngas quality is improved due to the RWGS reaction (Reaction 44) taking place within SOEC. Backward RWGS reaction is promoted with high H_2O mole fraction leading to positive RWGS reaction rate which consumes CO and increases H_2 mole fraction [17]. Therefore, at higher H_2O molar fraction, syngas production efficiency increases due to both higher H_2/CO_{out} and lower voltage/power utilisation. It was also observed that the average degradation rate is slightly higher for S1 than S2 (Table 6). Possible explanations might be that Ni sintering is enhanced with increased H_2O mole fraction (Equation 7) and/or Ni re-oxidation (Reaction 51) at the cathode [54].

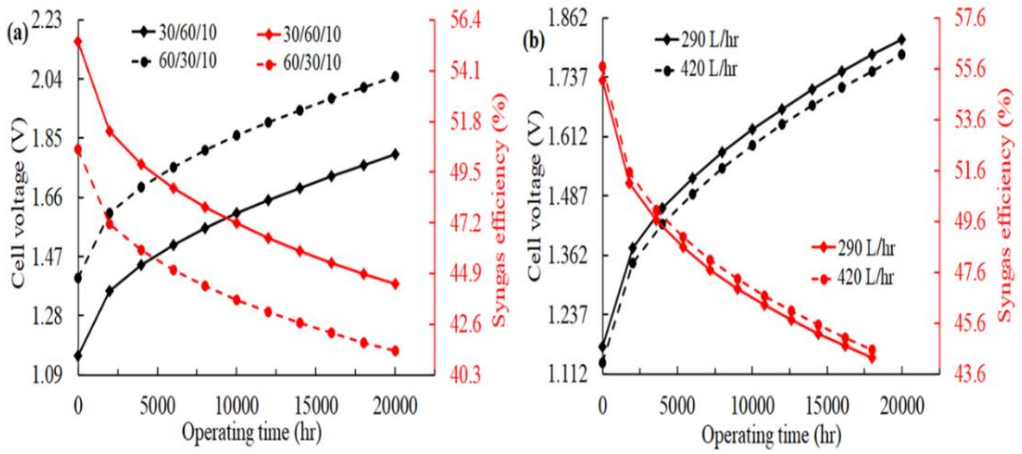

Figure 7: Evolution of SOEC voltage and syngas production efficiency for different (a) cathode feed gas composition given in $CO_2/H_2O/H_2$ (mol%) and (b) flowrate

Table 6: Simulation results for different feed compositions; S0: 45%CO_2/45%H_2O/10%H_2

	S0	**S1**	**S2**
H_2O/CO_{2in}	1.39	2.71	0.74
H_2/CO_{out}	1.07	1.99	0.59
U (V)	1.23	1.12	1.37
η_{syngas} (%)	53.1	55.4	50.5
$U_{20,000}$ (V)	1.91	1.80	2.05
Pcell (kW)	1.76	1.66	1.89
ΔU (%/1000hrs)	2.56	2.82	2.31

$$H_2O + 2Ni \rightleftharpoons Ni_2OH + 0.5H_2 \quad (51)$$

A rise in feed flowrate leads to higher syngas production efficiency (Figure 7b). This behaviour simply reflects the increased amount of reactants available at the TBP. This agrees with the findings of Menon et al. [22]. However, reactant conversion is limited by a given current density (Equation 45) leading to a decrease in required voltage decreases (Figure 7b) due to lower reactant conversion. This indicates that high feed flowrate may also result in reactant wastage thus, additional costs for raw materials and waste disposal.

5.4. Effect of structural degradation on SOEC long-term performance

5.4.1. Justification for case study

This section was added to understand the factors causing structural damages of SOEC materials and provide effective strategies to improve SOEC lifetime at high current density.

5.4.2. Setup of the case study

To carry out the case study, we assumed that when analysing one component material, the others remain unchanged. The following operating conditions were selected: 750 ℃, 1.5 A/cm^2, 30%CO_2/60%H_2O/10%H_2 and 360 L/hr cathode feed flowrate. The base case corresponds to Ni-YSZ/YSZ/LSM-YSZ properties provided in Tables 3 and 4. Characteristics of improved materials are specified in their corresponding sections.

5.4.3. Results and discussion

5.4.3.1. Cathode structural degradation

Figures 8a and 8b show the effects of Ni particle growth on the cathode TPB length, electronic conductivity and overpotential. Ni radius increases from 4.50 to 4.77 µm after 20,000 hours of operation. This results in a decrease in electronic conductivity and TPB length from 1,294 to 1,181 S/cm and 1.00 to 0.89, respectively. It is important to specify that TPB length value is given for $L_{TPB}/L_{TPB,0}$ ratio (Equation 13). The overall Ni agglomeration causes the cathodic overpotential to increase from 17.9 to 23.0 mV with an average cell degradation rate of 0.021%/1000hrs.

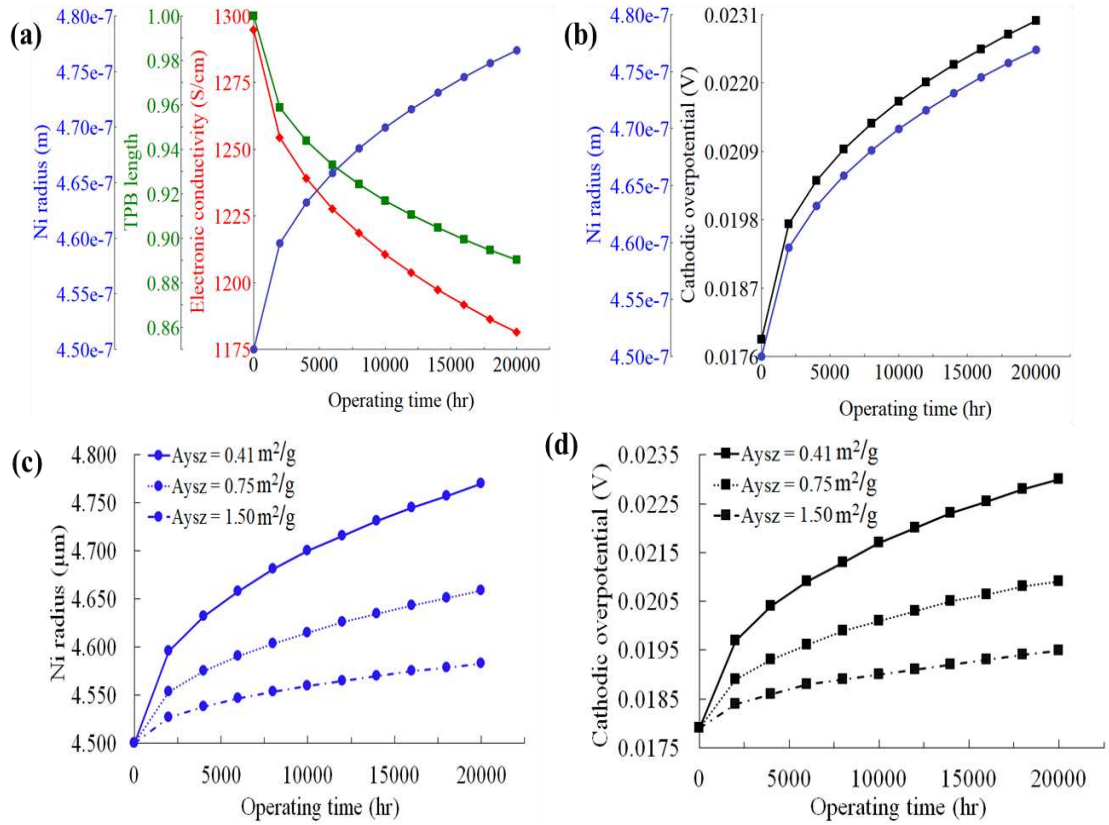

Figure 8: Effects of Ni particle growth on SOEC performance: (a) TPB length and conductivity; (b) cathodic overpotential; (c) and (d) Ni radius and cathodic overpotential for different YSZ surface area.

Various methods can be used to reduce Ni particle agglomeration including (according to Equation 8) reducing Ni/YSZ weight or volume ratio, increasing the initial Ni particle size and/or increasing YSZ surface area. However, decreasing Ni/YSZ volume ratio is undesirable as it may fasten the loss of electronic conductivity (Equations 20 to 24). Increasing the initial Ni particle size could increase the cathode porosity which may affect the mechanical strength and electronic conductivity due to lower connectivity between particles [38]. Hence, we focus on YSZ surface area to improve Ni-YSZ material.

YSZ surface area can be modified through the pre-calcination technique. Jia et al.[57] reported YSZ surface area of Ni-YSZ cermet between 0.48 to 2.43 m^2/g for raw and pre-calcined YSZ at 900–1200°C. Figure 8c depicts the evolution of Ni particle radius for different A_{YSZ} wherein 0.41 m^2/g is the base case used in Figures 8a and 8b. The cathodic overpotential is only 19.5 mV for

A_{YSZ} = 1.5 m^2/g after 20,000 hours of operation (Figure 8d). This is because YSZ acts as an inhibitor for Ni dispersion and sintering [57].

5.4.3.2. Electrolyte structural degradation

The effect of YSZ phase transition from cubic to tetragonal on the ionic conductivity and electrolyte overpotential is illustrated in Figure 9. YSZ ionic conductivity rapidly decreases from 0.0372 to 0.0291 S/cm the first 500 hours of operation and remain constant from 0.0289 S/cm. This agrees with experimental data reported for YSZ ionic conductivity using different Y_2O_3 mol% (2–10%) [58]. The associated overpotential follows the same trend and varies from 48.4 to 62.8 mV with a degradation rate of 0.06%/1000hrs after 20,000 hours of operation. The decrease in YSZ conductivity the first 500 hours is due to the short-range order-disorder transformation taking place in the crystal lattice. Because the oxygen ions are still able to easily diffuse after the transition period, YSZ conductivity remains stable once equilibrium is reached [58]. It is sensitive to conclude that YSZ electrolyte degradation does not significantly contribute to SOEC degradation regarding long-term performance since its ionic conductivity remains unchanged once the transition is completed.

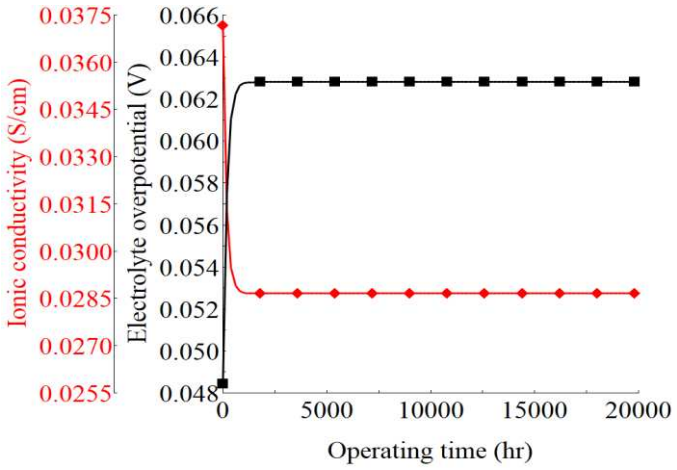

Figure 9: Impact of YSZ electrolyte phase transition on SOEC performance.

5.4.3.3. Anode structural degradation

Figures 10a and 10b illustrate the increase in ohmic and polarisation voltages associated with LSM-YSZ phase coarsening and the formation of LZO and COS layers for the base case. After 20,000

hours of operation, the ohmic voltage rises from 0 to 902.7 mV due to LZO and COS thickness growth from 0 to 1.4×10^{-4} cm and 0 to 2.3×10^{-3} cm, respectively. As the TBP length drops from 1.0 to 0.44, the polarisation voltage increases from 17.9 to 53.8 mV. The overall degradation rate is 3.96%/1000hrs. Therefore, long-term SOEC degradation is mostly due to LSM-YSZ anode delamination. The rate of COS growth can be lowered by applying anti-oxidant coating on the interconnect surface at the anode electrode side. When applying $La_{0.8}Sr_{0.2}CoO_3$ coating on the surface of Crofer 22 APU interconnect, $K_{g,COS}$ of the coated interconnect decreases from 2.40×10^{-9} to 1.15×10^{-10} $g^2/cm^4.hr$ [49]. COS thickness is now 5.0×10^{-4} cm after 20,000 hours of operation (Figure 10c) due to lower $K_{g,COS}$ obtained after coating.

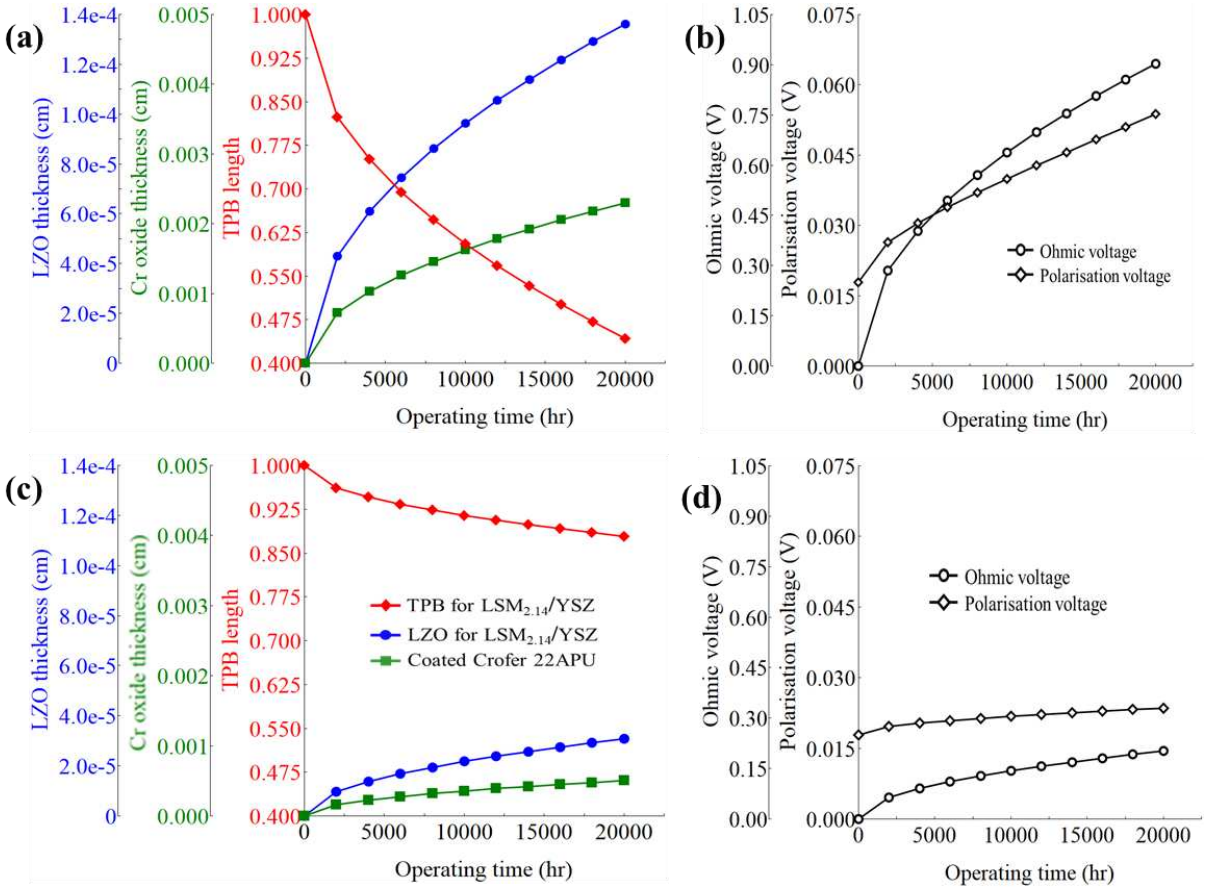

Figure 10: Effects of LSM-YSZ degradation on SOEC performance: (a) LZO thickness, Cr oxide thickness and TPB length for base case; (b) Ohmic and polarisation voltages associated with base case; (c) LZO thickness, Cr oxide thickness and TPB length for improved LSM-YSZ and (d) Ohmic and polarisation voltages associated with improved LSM-YSZ material.

LSM/YSZ with excess Mn and/or lower sintering temperatures can help to suppress or at least delay LZO growth. Excess Mn can be obtained by doping LSM with Mn or lowering La to Sr ratio in the A-site of LSM [48,59]. A-site deficient $La_{0.65}Sr_{0.3}MnO_3$/YSZ (La/Sr ratio = 2.14) sintered at 1000 ℃ achieved a $K_{g,LZO}$ of 2.26×10^{-3} $g^2/cm^4.hr$ [59]. This is lower than that of $(La_{0.75}Sr_{0.25})_{0.95}MnO_3$/YSZ (La/Sr ratio = 3.1) sintered at 1200℃ used for the base case. Applying $La_{0.65}Sr_{0.3}MnO_3$/YSZ material ($LSM_{2.14}$/YSZ), LZO thickness is only 3.1×10^{-5} cm after 20,000 hours of operation (Figure 10c). This is because LZO growth is controlled by Mn^{2+} diffusion and the surface diffusion constant is relatively low for $LSM_{2.14}$/YSZ material (5.76×10^{-11} cm^2/hr) [59]. Since LSM-YSZ phase coarsening is also controlled by Mn^{2+} diffusion (Section 2.4.3), TPB length evolution with operating time is also lower for $LSM_{2.14}$/YSZ material (Figure 10c). The ohmic and polarisation voltages of the improved LSM-YSZ material are reduced by 77.6% and 56.1% with an average degradation rate of 0.88%/1000hrs after 20,000 hours of operation (Figure 10d).

5.5. Overall SOEC performance and durability

The overall SOEC syngas production efficiency and performance degradation due to structural changes of Ni-YSZ/YSZ/LSM-YSZ material is presented in Figure 11. For the original SOEC, the syngas production efficiency decreases from 51.7 to 36.4% at 1.5 A/cm^2 after 20,000 hours of operation. The average degradation rate is 4.47%/1000 hours with 0.021%/1000hrs due to Ni agglomeration, 0.06%/1000hrs caused by YSZ electrolyte phase transition and 3.96%/1000hrs resulting from LSM-YSZ anode delamination. After optimisation of operating conditions and improvement of Ni-YSZ/YSZ/LSM-YSZ material set, the overall degradation rate is reduced to 0.89%/1000hrs with a syngas production efficiency varying from 54.1 to 49.9% after 20,000 hours of operation.

The above findings indicate that operating SOEC at adequate temperatures and cathode feed composition are essential for obtaining better degradation rate and enhancing syngas quality and production. The proper choice of Ni-YSZ cathode and LSM-YSZ anode compositions, as well as anti-oxidant coating of interconnects, are crucial for achieving low degradation rates. From this,

we can see that SOEC using conventional and low-cost materials can be sufficiently stable for large-scale application. Although the reported average degradation rate of 0.89%/1000hrs is below the target rate for commercialisation (1.0%/1000hrs), efforts are still needed to assess other sources of degradations such as mechanical failures and other component degradation (e.g. sealing). Furthermore, improved materials reported in this work have been experimentally tested for less than 1500 hours. Therefore, long-term degradation studies are required to fully assess the improved Ni-YSZ/YSZ/LSM-YSZ material stability.

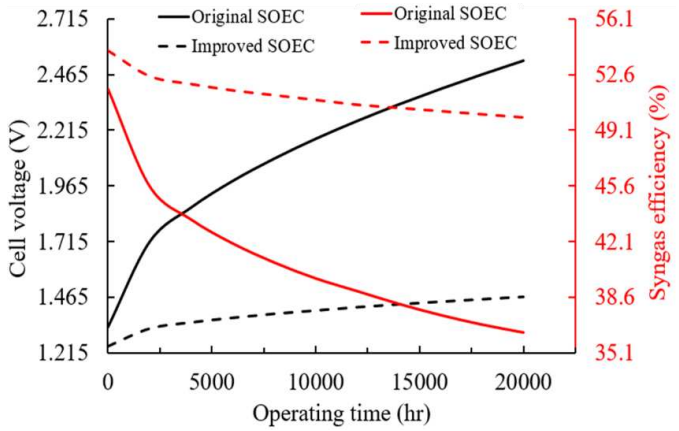

Figure 11: SOEC degradation and syngas production efficiency for the original and improved Ni-YSZ/YSZ/LSM-YSZ material set.

6. Conclusion

This paper presents a 1D pseudo-dynamic model of planar SOEC operating under CO_2/H_2O co-electrolysis. The model incorporates electrochemical reactions, mass transport and structural degradation of SOEC component materials. The developed model was validated in Aspen Plus® using Fortran® routines. The effects of operating conditions and structural degradation of Ni-YSZ cathode, YSZ electrolyte, LSM-YSZ anode and Crofer 22 APU interconnect materials on SOEC durability and syngas production efficiency were examined.

Lowering SOEC operating temperatures and cathode feed gas composition with higher H_2O content can help to reduce SOEC degradation rate and enhance the syngas production efficiency during long-term performance. YSZ electrolyte phase transition affects SOEC electrochemical

performance only during the first 500 hours of operation. The long-term degradation rate caused by Ni agglomeration at the cathode is 0.021%/1000hrs whereas, the degradation rate of 3.96%/1000hrs results from LSM-YSZ phase coarsening and growth of COS and LZO layers at the anode. The degradation rate at the anode can be reduced by 77.8% when coating $La_{0.8}Sr_{0.2}CoO_3$ anti-oxidant on the surface of Crofer 22 APU interconnect and adjusting La to Sr ratio in the A-site of LSM. The syngas efficiency of the original SOEC set drops from 51.7 to 36.4% at 1.5 A/cm^2 with an average degradation rate of 4.22%/1000hrs. The degradation rate of the improved SOEC material set is 0.89%/1000hrs after 20,000 hours of operation which is acceptable for commercial deployment.

Conflicts of interest

There are no conflicts to declare.

Acknowledgements

The first author would like to thank the University of Sheffield for partial PhD scholarship.

References

[1] C. Bu, D. Pallarès, X. Chen, A. Gómez-Barea, D. Liu, B. Leckner, P. Lu, Oxy-fuel combustion of a single fuel particle in a fluidized bed: Char combustion characteristics, an experimental study, Chem. Eng. J. 287 (2016) 649–656. https://doi.org/10.1016/j.cej.2015.11.078.

[2] Intergovernmental Panel on Climate Change, Special report - Global Warming of 1.5 ºC, (2018) 300. https://www.ipcc.ch/sr15 (accessed in January 5, 2021).

[3] J.P. Stempien, Q. Liu, M. Ni, Q. Sun, S.H. Chan, Physical principles for the calculation of equilibrium potential for co-electrolysis of steam and carbon dioxide in a Solid Oxide Electrolyzer Cell (SOEC), Electrochim. Acta. 147 (2014) 490–497. https://doi.org/10.1016/J.ELECTACTA.2014.09.144.

[4] C. Graves, S.D. Ebbesen, M. Mogensen, Co-electrolysis of CO_2 and H_2O in solid oxide cells: Performance and durability, Solid State Ionics. 192 (2011) 398–403. https://doi.org/10.1016/J.SSI.2010.06.014.

[5] Y. Zheng, J. Wang, B. Yu, W. Zhang, J. Chen, J. Qiao, J. Zhang, A review of high temperature co-electrolysis of H_2O and CO_2 to produce sustainable fuels using solid oxide electrolysis cells (SOECs): Advanced materials and technology, Chem. Soc. Rev. 46 (2017) 1427–1463. https://doi.org/10.1039/c6cs00403b.

[6] R. Boehm, H. Yang, J. Yan, Handbook of clean energy systems – Volume 5: Energy storage, Wiley, Chichester, 2015.

[7] S.D. Ebbesen, C. Graves, M. Mogensen, Production of synthetic fuels by co-electrolysis of steam and carbon dioxide, Int. J. Green Energy. 6 (2009) 646–660. https://doi.org/10.1080/15435070903372577.

[8] X. Sun, M. Chen, Y.-L. Liu, P. Hjalmarsson, S.D. Ebbesen, S.H. Jensen, M.B. Mogensen, P.V. Hendriksen, Durability of Solid Oxide Electrolysis Cells for Syngas Production, J.

Electrochem. Soc. 160 (2013) F1074–F1080. https://doi.org/10.1149/2.106309jes.

[9] X. Chen, C. Guan, G. Xiao, X. Du, J.Q. Wang, Syngas production by high temperature steam/CO_2 coelectrolysis using solid oxide electrolysis cells, Faraday Discuss. 182 (2015) 341–351. https://doi.org/10.1039/c5fd00017c.

[10] M.T. Mehran, S.-B. Yu, D.-Y. Lee, J.-E. Hong, S.-B. Lee, S.-J. Park, R.-H. Song, T.-H. Lim, Production of syngas from H_2O/CO_2 by high-pressure coelectrolysis in tubular solid oxide cells, Appl. Energy. 212 (2018) 759–770. https://doi.org/10.1016/J.APENERGY.2017.12.078.

[11] S.-B. Yu, S.-H. Lee, M.T. Mehran, J.-E. Hong, J.-W. Lee, S.-B. Lee, S.-J. Park, R.-H. Song, J.-H. Shim, Y.-G. Shul, T.-H. Lim, Syngas production in high performing tubular solid oxide cells by using high-temperature H_2O/CO_2 co-electrolysis, Chem. Eng. J. 335 (2018) 41–51. https://doi.org/10.1016/J.CEJ.2017.10.110.

[12] S. Diethelm, J. Van Herle, D. Montinaro, O. Bucheli, Electrolysis and Co-electrolysis performance of SOE short stacks, Fuel Cells. 13 (2013) 631–637. https://doi.org/10.1002/fuce.201200178.

[13] M. Kotisaari, O. Thomann, D. Montinaro, J. Kiviaho, Evaluation of a SOE Stack for Hydrogen and Syngas Production: a Performance and Durability Analysis, Fuel Cells. 17 (2017) 571–580. https://doi.org/10.1002/fuce.201600166.

[14] C.M. Stoots, J.E. O'Brien, J.S. Herring, J.J. Hartvigsen, Syngas production via high-temperature coelectrolysis of steam and carbon dioxide, J. Fuel Cell Sci. Technol. 6 (2009) 0110141–01101412. https://doi.org/10.1115/1.2971061.

[15] C.M. Stoots, J.E. O'Brien, K.G. Condie, J.J. Hartvigsen, High-temperature electrolysis for large-scale hydrogen production from nuclear energy – Experimental investigations, Int. J. Hydrogen Energy. 35 (2010) 4861–4870. https://doi.org/10.1016/J.IJHYDENE.2009.10.045.

[16] M. Reytier, S. Di Iorio, A. Chatroux, M. Petitjean, J. Cren, M. De Saint Jean, J. Aicart, J.

Mougin, Stack performances in high temperature steam electrolysis and co-electrolysis, Int. J. Hydrogen Energy. 40 (2015) 11370–11377. https://doi.org/10.1016/J.IJHYDENE.2015.04.085.

[17] M. Ni, 2D thermal modeling of a solid oxide electrolyzer cell (SOEC) for syngas production by H_2O/CO_2 co-electrolysis, Int. J. Hydrogen Energy. 37 (2012) 6389–6399. https://doi.org/10.1016/J.IJHYDENE.2012.01.072.

[18] M. Ni, An electrochemical model for syngas production by co-electrolysis of H_2O and CO_2, J. Power Sources. 202 (2012) 209–216. https://doi.org/10.1016/j.jpowsour.2011.11.080.

[19] Y. Xie, X. Xue, Modeling of solid oxide electrolysis cell for syngas generation with detailed surface chemistry, Solid State Ionics. 224 (2012) 64–73. https://doi.org/10.1016/J.SSI.2012.07.015.

[20] J.P. Stempien, Q. Sun, S.H. Chan, Performance of power generation extension system based on solid-oxide electrolyzer cells under various design conditions, Energy. 55 (2013) 647–657. https://doi.org/10.1016/J.ENERGY.2013.03.031.

[21] Y. Luo, Y. Shi, W. Li, N. Cai, Comprehensive modeling of tubular solid oxide electrolysis cell for co-electrolysis of steam and carbon dioxide, Energy. 70 (2014) 420–434. https://doi.org/10.1016/J.ENERGY.2014.04.019.

[22] V. Menon, Q. Fu, V.M. Janardhanan, O. Deutschmann, A model-based understanding of solid-oxide electrolysis cells (SOECs) for syngas production by H_2O/CO_2 co-electrolysis, J. Power Sources. 274 (2015) 768–781. https://doi.org/10.1016/J.JPOWSOUR.2014.09.158.

[23] G. Hawkes, J. O'Brien, C. Stoots, S. Herring, R. Jones, Three Dimensional CFD Model of a Planar Solid Oxide Electrolysis Cell for Co-Electrolysis of Steam and Carbon Dioxide, in: Fuel Cell Semin., Honolulu, 2006: p. 911874.

[24] Y. Zheng, Y. Luo, Y. Shi, N. Cai, Dynamic Processes of Mode Switching in Reversible Solid Oxide Fuel Cells, J. Energy Eng. 143 (2017) 1–8.

https://doi.org/10.1061/(ASCE)EY.1943-7897.0000482.

[25] Y. Luo, Y. Shi, W. Li, N. Cai, Dynamic electro-thermal modeling of co-electrolysis of steam and carbon dioxide in a tubular solid oxide electrolysis cell, Energy. 89 (2015) 637–647. https://doi.org/10.1016/J.ENERGY.2015.05.150.

[26] A. Banerjee, Y. Wang, J. Diercks, O. Deutschmann, Hierarchical modeling of solid oxide cells and stacks producing syngas via H_2O/CO_2 Co-electrolysis for industrial applications, Appl. Energy. 230 (2018) 996–1013. https://doi.org/10.1016/J.APENERGY.2018.08.122.

[27] A.D.N. Kamkeng, M. Wang, J. Hu, W. Du, F. Qian, Transformation technologies for CO_2 utilisation: Current status, challenges and future prospects, Chem. Eng. J. 409 (2021) 128138. https://doi.org/10.1016/j.cej.2020.128138.

[28] P. Moçoteguy, A. Brisse, A review and comprehensive analysis of degradation mechanisms of solid oxide electrolysis cells, Int. J. Hydrogen Energy. 38 (2013) 15887–15902. https://doi.org/10.1016/J.IJHYDENE.2013.09.045.

[29] A. V. Virkar, Mechanism of oxygen electrode delamination in solid oxide electrolyzer cells, Int. J. Hydrogen Energy. 35 (2010) 9527–9543. https://doi.org/10.1016/J.IJHYDENE.2010.06.058.

[30] M. Nerat, Đ. Juričić, Modelling of anode delamination in solid oxide electrolysis cell and analysis of its effects on electrochemical performance, Int. J. Hydrogen Energy. 43 (2018) 8179–8189. https://doi.org/10.1016/J.IJHYDENE.2018.02.189.

[31] C. Graves, S.D. Ebbesen, S.H. Jensen, S.B. Simonsen, M.B. Mogensen, Eliminating degradation in solid oxide electrochemical cells by reversible operation, Nat. Mater. 14 (2015) 239–244. https://doi.org/10.1038/nmat4165.

[32] S.D. Ebbesen, J. Høgh, K.A. Nielsen, J.U. Nielsen, M. Mogensen, Durable SOC stacks for production of hydrogen and synthesis gas by high temperature electrolysis, Int. J. Hydrogen Energy. 36 (2011) 7363–7373. https://doi.org/10.1016/J.IJHYDENE.2011.03.130.

[33] M. Chen, Y.-L. Liu, J.J. Bentzen, W. Zhang, X. Sun, A. Hauch, Y. Tao, J.R. Bowen, P.V. Hendriksen, Microstructural Degradation of Ni/YSZ Electrodes in Solid Oxide Electrolysis Cells under High Current, J. Electrochem. Soc. 160 (2013) F883–F891. https://doi.org/10.1149/2.098308jes.

[34] C. Chatzichristodoulou, M. Chen, P.V. Hendriksen, T. Jacobsen, M.B. Mogensen, Understanding degradation of solid oxide electrolysis cells through modeling of electrochemical potential profiles, Electrochim. Acta. 189 (2016) 265–282. https://doi.org/10.1016/J.ELECTACTA.2015.12.067.

[35] M. Navasa, C. Graves, C. Chatzichristodoulou, T. Løye Skafte, B. Sundén, H. Lund Frandsen, A three dimensional multiphysics model of a solid oxide electrochemical cell: A tool for understanding degradation, Int. J. Hydrogen Energy. 43 (2018) 11913–11931. https://doi.org/10.1016/J.IJHYDENE.2018.04.164.

[36] L. Wang, M. Chen, R. Küngas, T.-E. Lin, S. Diethelm, F. Maréchal, J. Van herle, Power-to-fuels via solid-oxide electrolyzer: Operating window and techno-economics, Renew. Sustain. Energy Rev. 110 (2019) 174–187. https://doi.org/10.1016/J.RSER.2019.04.071.

[37] M.S. Sohal, J.E. O'Brien, C.M. Stoots, V.I. Sharma, B. Yildiz, A. Virkar, Degradation issues in solid oxide cells during high temperature electrolysis, J. Fuel Cell Sci. Technol. 9 (2012) 1–10. https://doi.org/10.1115/1.4003787.

[38] A. Faes, A. Hessler-Wyser, D. Presvytes, C.G. Vayenas, J. Vanherle, Nickel-zirconia anode degradation and triple phase boundary quantification from microstructural analysis, Fuel Cells. 9 (2009) 841–851. https://doi.org/10.1002/fuce.200800147.

[39] J. Sehested, Sintering of nickel steam-reforming catalysts, J. Catal. 217 (2003) 417–426. https://doi.org/10.1016/S0021-9517(03)00075-7.

[40] J. Sehested, J.A.P. Gelten, S. Helveg, Sintering of nickel catalysts: Effects of time, atmosphere, temperature, nickel-carrier interactions, and dopants, Appl. Catal. A Gen. 309

(2006) 237–246. https://doi.org/10.1016/j.apcata.2006.05.017.

[41] R.M.C. Clemmer, S.F. Corbin, The influence of pore and Ni morphology on the electrical conductivity of porous Ni/YSZ composite anodes for use in solid oxide fuel cell applications, Solid State Ionics. 180 (2009) 721–730. https://doi.org/10.1016/j.ssi.2009.02.030.

[42] J. Wu, D.S. McLachlan, Percolation exponents and thresholds in two nearly ideal anisotropic continuum systems, Phys. Rev. B. 56 (1997) 1236–1248. https://doi.org/10.1016/S0378-4371(97)00108-8.

[43] D. Chen, Z. Lin, H. Zhu, R.J. Kee, Percolation theory to predict effective properties of solid oxide fuel-cell composite electrodes, J. Power Sources. 191 (2009) 240–252. https://doi.org/10.1016/j.jpowsour.2009.02.051.

[44] M. Hattori, Y. Takeda, Y. Sakaki, A. Nakanishi, S. Ohara, K. Mukai, J.H. Lee, T. Fukui, Effect of aging on conductivity of yttria stabilized zirconia, J. Power Sources. 126 (2004) 23–27. https://doi.org/10.1016/j.jpowsour.2003.08.018.

[45] N. Jiang, E.D. Wachsman, Structural Stability and Conductivity of Phase-Stabilized Cubic Bismuth Oxides, J. Am. Ceram. Soc. 82 (1999) 3057–3064.

[46] A.S. Farlenkov, M. V. Ananyev, V.A. Eremin, N.M. Porotnikova, E.K.H. Kurumchin, Particle coarsening influence on oxygen reduction in LSM-YSZ composite materials, Fuel Cells. 15 (2015) 131–139. https://doi.org/10.1002/fuce.201400106.

[47] M. Keane, M.K. Mahapatra, A. Verma, P. Singh, LSM-YSZ interactions and anode delamination in solid oxide electrolysis cells, Int. J. Hydrogen Energy. 37 (2012) 16776–16785. https://doi.org/10.1016/j.ijhydene.2012.08.104.

[48] A. Mitterdorfer, L.J. Gauckler, $La_2Zr_2O_7$ formation and oxygen reduction kinetics of the La0.85Sr0.15MnyO3, O2(g)|YSZ system, Solid State Ionics. 111 (1998) 185–218. https://doi.org/10.1016/s0167-2738(98)00195-7.

[49] M. Palcut, L. Mikkelsen, K. Neufeld, M. Chen, R. Knibbe, P.V. Hendriksen, Improved

oxidation resistance of ferritic steels with LSM coating for high temperature electrochemical applications, Int. J. Hydrogen Energy. 37 (2012) 8087–8094. https://doi.org/10.1016/j.ijhydene.2011.11.138.

[50] D. Larrain, J. Van herle, D. Favrat, Simulation of SOFC stack and repeat elements including interconnect degradation and anode reoxidation risk, J. Power Sources. 161 (2006) 392–403. https://doi.org/10.1016/j.jpowsour.2006.04.151.

[51] Y.L. Liu, K. Thydén, M. Chen, A. Hagen, Microstructure degradation of LSM-YSZ cathode in SOFCs operated at various conditions, Solid State Ionics. 206 (2012) 97–103. https://doi.org/10.1016/j.ssi.2011.10.020.

[52] J. Crank, The Mathematics of Diffusion, 2nd ed., Oxford University Press, London, 1975. https://doi.org/10.1021/ja01562a072.

[53] G. Cinti, G. Discepoli, G. Bidini, A. Lazini, M. Santarelli, Co-electrolysis of water and CO_2 in a solid oxide electrolyzer (SOE) stack, Int. J. Energy Res. 40 (2016) 207–215. https://doi.org/10.1002/er.3450.

[54] J. Sehested, J.A.P. Gelten, I.N. Remediakis, H. Bengaard, J.K. Nørskov, Sintering of nickel steam-reforming catalysts: effects of temperature and steam and hydrogen pressures, J. Catal. 223 (2004) 432–443. https://doi.org/10.1016/J.JCAT.2004.01.026.

[55] B. Li, X. Fan, K. Zhou, T.J. Wang, Effect of oxide growth on the stress development in double-ceramic-layer thermal barrier coatings, Ceram. Int. 43 (2017) 14763–14774. https://doi.org/10.1016/j.ceramint.2017.07.218.

[56] M. Lang, C. Bohn, K. Couturier, X. Sun, S.J. McPhail, T. Malkow, A. Pilenga, Q. Fu, Q. Liu, Electrochemical Quality Assurance of Solid Oxide Electrolyser (SOEC) Stacks, J. Electrochem. Soc. 166 (2019) F1180–F1189. https://doi.org/10.1149/2.0041915jes.

[57] L. Jia, Z. Lu, J. Miao, Z. Liu, G. Li, W. Su, Effects of pre-calcined YSZ powders at different temperatures on Ni-YSZ anodes for SOFC, J. Alloys Compd. 414 (2006) 152–157.

https://doi.org/10.1016/j.jallcom.2005.03.119.

[58] J. Kondoh, T. Kawashima, S. Kikuchi, Y. Tomii, Y. Ito, Effect of Aging on Yltria-Stabilized Zirconia, J. Electrochem. Soc. 145 (1995) 1527–1536.

[59] C.T. Yang, W.J. Wei, A. Roosen, Reaction Kinetics and Mechanisms between $La_{0.65}Sr_{0.3}MnO_3$ and 8 mol% Yttria-Stabilized Zirconia, J. Am. Ceram. Soc. 7 (2004) 1110–1116.